ANGLES-ONLY TRACKING AND NAVIGATION FOR APPROACH AND RENDEZVOUS IN GEOSYNCHRONOUS ORBITS

Justin Kruger[*], Simone D'Amico [†], Christopher Roscoe [‡] and Jason Westphal [§]

Onboard relative navigation for geosynchronous rendezvous using vision-based sensors poses unique challenges for target tracking and orbit determination algorithms. Uncertainties in a priori state information require intelligent methods for discriminating potentially non-cooperative targets amongst multiple dynamically similar objects. Tracking is needed during fast rendezvous approaches and continuous thrusting arcs, presenting challenging angles-only observability. This paper describes usage of new on-board tracking models, short-arc orbit determination methods, and system state augmentations to extend an angles-only navigation architecture to the geosynchronous environment. High-fidelity simulations of single-observer rendezvous and multi-observer target tracking demonstrate robust performance in support of autonomous satellite inspection and servicing.

INTRODUCTION

In recent years, there has been immense growth in usage of the space environment, driving a need for greater efficiency in how satellite vehicles are leveraged and maintained.[1] Satellite lifetimes in orbit are currently limited by finite on-board fuel resources or hardware degradation and failure, and it is desirable to be able to service or refuel target satellites to extend their lifetime in a more sustainable fashion. Of particular focus is servicing for satellites in geosynchronous orbits (GEO).[2] Such satellites are often very large, expensive, and tasked with fulfilling critical long-term objectives, and slots for additional satellites in the GEO belt are limited. A variety of mission concepts have been proposed for this purpose.[3–6]

To enable rendezvous with a desired target, it is necessary to be able to characterize the object and robustly determine its relative orbit during a servicer's approach. However, target satellites may be known versus unknown, or cooperative versus uncooperative, which creates navigation challenges. External measurement sources such as Global Navigation Satellite System (GNSS) signals, and cooperative measurements such as inter-satellite ranging, may be unavailable for targets of interest. Radar, lidar and related techniques are generally inappropriate for spacecraft due to their complexity, mass and power requirements. In addition, relying on ground support for orbit determination possesses limited scalability and reduces autonomy and responsiveness on orbit.

A potential solution is angles-only navigation, in which observer satellites use on-board vision-based sensors (VBS) to obtain bearing angles to target space objects. Benefits of the angles-only approach are that it is passive and can navigate for non-cooperative targets; the ubiquity, accuracy and robustness of cameras; and a reliance on on-board measurements rather than external resources. Conversely, optical measurements are affected by physical target visibility constraints, and bearing angles do not provide explicit target range

---

[*]Ph. D. Candidate, Stanford University, Department of Aeronautics and Astronautics, Space Rendezvous Laboratory, Durand Building, 496 Lomita Mall, Stanford, CA 94305.

[†]Associate Professor, Stanford University, Department of Aeronautics and Astronautics, Space Rendezvous Laboratory, Durand Building, 496 Lomita Mall, Stanford, CA 94305.

[‡]Co-Founder, Ten One Aerospace, Washington, DC.

[§]Co-Founder, Ten One Aerospace, Washington, DC.

information. This leads to complex relationships between state observability and measurements as well as weakly observable system modes.[7–9]

The feasibility of angles-only navigation in orbit has been demonstrated by two prior flight experiments. In 2012, the Advanced Rendezvous using GPS and Optical Navigation (ARGON) experiment enabled the rendezvous of two smallsats in Low Earth Orbit (LEO) from inter-satellite separations of 30 km to 3 km.[10] Subsequently, the Autonomous Vision Approach Navigation and Target Identification (AVANTI) experiment conducted a rendezvous of two smallsats from separations of 13 km to 50 m[11] in 2016. Although both experiments were successful, they are characterized by four key deficiencies: 1) inability to accommodate multiple observers and targets 2) reliance on accurate a-priori relative orbit information for initialization, 3) reliance on external knowledge of the observer's absolute orbit to maintain state convergence, and 4) reliance on frequent translational maneuvers to resolve the weakly observable range to the target.

In response, Stanford's Space Rendezvous Laboratory (SLAB) has proposed the Absolute and Relative Trajectory Measurement System (ARTMS)[12].[13] ARTMS is an autonomous angles-only navigation architecture for multi-agent space systems divided into three modules and corresponding new algorithms: IMage Processing (IMP),[14] Batch Orbit Determination (BOD),[15] and Sequential Orbit Determination (SOD).[12] IMP identifies multiple resident space objects (RSO) in 2D images from a single monocular camera without requiring a-priori relative orbit knowledge. BOD generates an initial state estimate for all participating satellites by using batches of angles to targets and a single coarse absolute orbit initialization for the observer. SOD continually refines the ARTMS state estimate using an adaptive and efficient unscented Kalman filter (UKF), fusing measurements from multiple observers broadcast over an inter-satellite link (ISL). In this fashion, ARTMS enables distributed, autonomous, and scalable angles-only navigation with minimal reliance on external or a-priori information and no reliance on maneuvers.

ARTMS is due to be flight-tested in LEO during the Starling Formation-flying Optical eXperiment (Star-FOX).[16] StarFOX is a core payload of the upcoming NASA Starling mission, a technology demonstration consisting of four CubeSats scheduled for launch in 2023. The use of ARTMS to support navigation in deep space has also been studied in the form of high-fidelity simulations in lunar and Martian environments.[17,18]

This paper explores the applicability and extension of ARTMS to angles-only navigation in GEO, with a focus on target characterization and rendezvous during servicing scenarios. Significant algorithmic modifications are needed, given that ARTMS was initially developed for a LEO swarm experiment with relatively static inter-satellite spacings. Similarities in dynamics amongst objects in the GEO belt require intelligent methods for discriminating between multiple simultaneous object detections when acquiring desired targets, based on a priori states which are uncertain or unknown. Tracking must also be maintained during both fast approach maneuvers and long-duration thrusting arcs by the observer. Angles-only observability must be carefully accounted for, given the long-term perturbing effects of forces such as solar radiation pressure (SRP).

To address these concerns, this work extends ARTMS with several algorithmic developments, including 1) new tracking and identification modes in IMP for increased precision during target acquisition; 2) exploration of new second-order dynamics models and fast initial relative orbit determination methods for BOD; and 3) augmentation of estimated states for more autonomy and robustness in SOD. Algorithms are validated with high-fidelity simulations of several target characterization and rendezvous scenarios in GEO, using the ARTMS flight software framework. The potential of autonomous distributed angles-only navigation for enabling and supporting satellite inspection and servicing in GEO is demonstrated.

The paper is organized as follows. First, the mathematical background of the ARTMS measurement model, dynamics model, and estimated state is presented. This is followed by an introduction to the ARTMS architecture and core algorithms, as well as algorithmic modifications to allow ARTMS to operate in GEO. Simulation scenarios and the data generation pipeline are then detailed, along with a discussion of results. The final section contains concluding remarks.

MODELING PRELIMINARIES

Measurement Model

ARTMS produces angles-only measurements by computing time-tagged bearing angles to objects detected in VBS images. First, define the radial/along-track/cross-track (RTN) frame of the observer, denoted $\mathcal{R}$. It is centered on and rotates with the observer and consists of orthogonal basis vectors $\hat{\boldsymbol{x}}^{\mathcal{R}}$ (directed along the observer's absolute position vector); $\hat{\boldsymbol{z}}^{\mathcal{R}}$ (directed along the observer's orbital angular momentum vector); and $\hat{\boldsymbol{y}}^{\mathcal{R}} = \hat{\boldsymbol{z}}^{\mathcal{R}} \times \hat{\boldsymbol{x}}^{\mathcal{R}}$.[19] Similarly, define a frame $\mathcal{W}$ using $\hat{\boldsymbol{y}}^{\mathcal{W}}$ (directed along the observer's velocity vector); $\hat{\boldsymbol{z}}^{\mathcal{W}} = \hat{\boldsymbol{z}}^{\mathcal{R}}$; and $\hat{\boldsymbol{x}}^{\mathcal{W}} = \hat{\boldsymbol{y}}^{\mathcal{W}} \times \hat{\boldsymbol{z}}^{\mathcal{W}}$. $\mathcal{W}$ only differs from $\mathcal{R}$ by a rotation of the observer flight path angle ϕ_f about $\hat{\boldsymbol{z}}^{\mathcal{R}}$ with $\phi_f \approx 0$ in near-circular orbits.[19] Bearing angles consist of azimuth and elevation (α, ϵ) and subtend the LOS vector $\delta \boldsymbol{r}^{\mathcal{V}} = (\delta r_x^{\mathcal{V}}, \delta r_y^{\mathcal{V}}, \delta r_z^{\mathcal{V}})$ from the observer to the target. Superscript $\mathcal{V}$ indicates description in the observer VBS coordinate frame, consisting of orthogonal basis vectors $\hat{\boldsymbol{x}}^{\mathcal{V}}, \hat{\boldsymbol{y}}^{\mathcal{V}}, \hat{\boldsymbol{z}}^{\mathcal{V}}$, such that $\hat{\boldsymbol{z}}^{\mathcal{V}}$ is directed along the camera boresight. The VBS may be aligned as necessary to keep swarm targets in the field of view (FOV). Bearing angles are then computed via[12]

$$\begin{pmatrix} \alpha \\ \epsilon \end{pmatrix}^{\mathcal{V}} = \begin{pmatrix} \arcsin \delta r_y^{\mathcal{V}} / ||\delta \boldsymbol{r}^{\mathcal{V}}||_2 \\ \arctan \delta r_x^{\mathcal{V}} / \delta r_z^{\mathcal{V}} \end{pmatrix} \tag{1}$$

Bearing angles can be related to the inertial frame by rotating $\delta \boldsymbol{r}^{\mathcal{V}}$ into the Earth-Centered Inertial (ECI) frame $\mathcal{I}$, as per

$$\delta \boldsymbol{r}^{\mathcal{I}} = {}^{\mathcal{V}}\overrightarrow{\boldsymbol{R}}^{\mathcal{I}} \delta \boldsymbol{r}^{\mathcal{V}} \tag{2}$$

where ${}^{\mathcal{V}}\overrightarrow{\boldsymbol{R}}^{\mathcal{I}}$ denotes a rotation from frame $\mathcal{V}$ into frame $\mathcal{I}$. This rotation matrix is computed by performing attitude determination using stars identified by the VBS.[10] Rotation matrices ${}^{\mathcal{R}}\overrightarrow{\boldsymbol{R}}^{\mathcal{I}}$ and ${}^{\mathcal{W}}\overrightarrow{\boldsymbol{R}}^{\mathcal{I}}$ can be computed using the observer's absolute orbit estimate. Figure 1 depicts the relationship between coordinate frames and bearing angles.
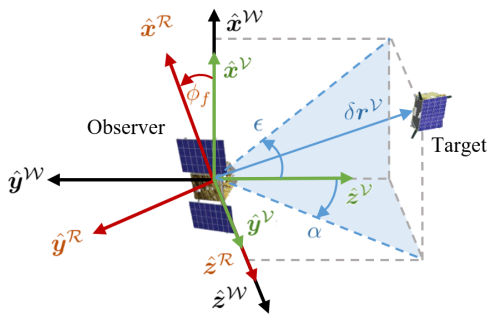

Figure 1: Definition of target bearing angles with respect to $\mathcal{V}, \mathcal{R}$ and $\mathcal{W}$, with the VBS pointing in the anti-velocity direction.
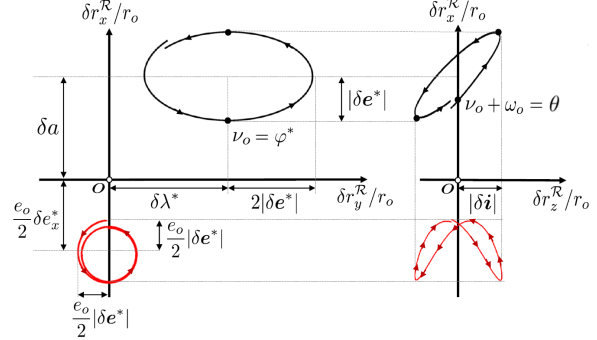

Figure 2: Target relative motion in the $\hat{\boldsymbol{x}}^{\mathcal{R}}$-$\hat{\boldsymbol{y}}^{\mathcal{R}}$ (RT) and $\hat{\boldsymbol{x}}^{\mathcal{R}}$-$\hat{\boldsymbol{z}}^{\mathcal{R}}$ (RN) planes. Motion first-order in spacecraft separation is in black. Motion proportional to e is in red.[12]

State Parametrization

ARTMS represents the absolute state $\boldsymbol{\alpha}$ of the observer in terms of orbit elements (OE), which may be either quasi-nonsingular (QNS) or nonsingular (NS). The quasi-nonsingular OE possess a singularity when the orbit inclination is zero whereas the nonsingular OE do not.[19] The nonsingular OE are therefore applicable to navigation for geosynchronous orbits, which are typically equatorial.

$$\boldsymbol{\alpha}_{\text{QNS}} = \begin{pmatrix} a \\ e_x \\ e_y \\ i \\ \Omega \\ u \end{pmatrix} = \begin{pmatrix} a \\ e \cos \omega \\ e \sin \omega \\ i \\ \Omega \\ \omega + M \end{pmatrix} \qquad \boldsymbol{\alpha}_{\text{NS}} = \begin{pmatrix} p \\ f \\ g \\ h \\ k \\ L \end{pmatrix} = \begin{pmatrix} a(1 - e^2) \\ e \cos (\omega + \Omega) \\ e \sin (\omega + \Omega) \\ \tan (i/2) \cos \Omega \\ \tan (i/2) \sin \Omega \\ \omega + \Omega + M \end{pmatrix} \tag{3}$$

Above, a, e, i, Ω, ω, and M are the canonical Keplerian OE of semi-major axis, eccentricity, inclination, right ascension of the ascending node, argument of periapsis, and mean anomaly respectively. Additionally, p is the semilatus rectum, u is the mean argument of latitude, and L is the mean longitude. All are computed with respect to $\mathcal{I}$.

The relative orbit $\delta\boldsymbol{\alpha}$ of a target spacecraft, as tracked by an observer, is described by relative orbit elements (ROE).[20,21] The ROE state parametrization may be QNS or NS, with the nonsingular ROE avoiding singularities at zero inclination. The ROE are defined in terms of the absolute OE of the observer and target (denoted by subscripts 'o' and 't' respectively) via

$$\delta\boldsymbol{\alpha}_{\text{QNS}} = \begin{pmatrix} \delta a \\ \delta\lambda \\ \delta e_x \\ \delta e_y \\ \delta i_x \\ \delta i_y \end{pmatrix} = \begin{pmatrix} \delta a \\ \delta\lambda \\ |\delta\boldsymbol{e}| \cos \varphi \\ |\delta\boldsymbol{e}| \sin \varphi \\ |\delta\boldsymbol{i}| \cos \vartheta \\ |\delta\boldsymbol{i}| \sin \vartheta \end{pmatrix} = \begin{pmatrix} (a_t - a_o)/a_o \\ (u_t - u_o) + (\Omega_t - \Omega_o) \cos i_o \\ e_{x,t} - e_{x,o} \\ e_{y,t} - e_{y,o} \\ i_t - i_o \\ (\Omega_t - \Omega_o) \sin i_o \end{pmatrix} \qquad \delta\boldsymbol{\alpha}_{\text{NS}} = \begin{pmatrix} \delta a \\ \delta L \\ \delta f \\ \delta g \\ \delta h \\ \delta k \end{pmatrix} = \begin{pmatrix} (a_t - a_o)/a_o \\ L_t - L_o \\ f_t - f_o \\ g_t - g_o \\ h_t - h_o \\ k_t - k_o \end{pmatrix} \tag{4}$$

Above, δa is the relative semi-major axis, $\delta\lambda$ is the relative mean longitude, $\delta\boldsymbol{e} = (\delta e_x, \delta e_y)$ is the relative eccentricity vector with magnitude δe and phase φ, and $\delta\boldsymbol{i} = (\delta i_x, \delta i_y)$ is the relative inclination vector with magnitude δi and phase ϑ.

The ARTMS state also includes several optional components. First are absolute empirical accelerations for the observer and differential empirical accelerations for targets, defined as

$$\boldsymbol{a}_{\text{emp}}^{\mathcal{R}} = \begin{pmatrix} a_x \\ a_y \\ a_z \end{pmatrix}^{\mathcal{R}} \qquad \delta\boldsymbol{a}_{\text{emp}}^{\mathcal{R}} = \begin{pmatrix} \delta a_x \\ \delta a_y \\ \delta a_z \end{pmatrix}^{\mathcal{R}} = \begin{pmatrix} a_{x,t} - a_{x,o} \\ a_{y,t} - a_{y,o} \\ a_{z,t} - a_{z,o} \end{pmatrix}^{\mathcal{R}} \tag{5}$$

respectively in $\mathcal{R}$. Empirical accelerations are used to approximately capture unmodeled dynamics, and are more computationally efficient than numerically integrating the full differential equations of relative motion.[22] The absolute ballistic coefficient of the observer and differential ballistic coefficients of targets with respect to the observer can also be estimated, denoted as

$$\boldsymbol{B} = \begin{pmatrix} B_{\text{atm}} \\ B_{\text{srp}} \end{pmatrix} \qquad \delta\boldsymbol{B} = \begin{pmatrix} \delta B_{\text{atm}} \\ \delta B_{\text{srp}} \end{pmatrix} = \begin{pmatrix} B_{\text{atm},t} - B_{\text{atm},o} \\ B_{\text{srp},t} - B_{\text{srp},o} \end{pmatrix} \tag{6}$$

For the GEO case, only the SRP coefficient is taken into account. Additional state components such as clock errors, clock drift rates and VBS sensor biases can be estimated by ARTMS[12,17] but are not included here. Thus, for the observer and n tracked targets, the complete ARTMS state is

$$\boldsymbol{x} = (\boldsymbol{\alpha}, \boldsymbol{a}, \boldsymbol{B}, \delta\boldsymbol{\alpha}_1, \delta\boldsymbol{a}_1, \delta\boldsymbol{B}_1 ..., \delta\boldsymbol{\alpha}_n, \delta\boldsymbol{a}_n, \delta\boldsymbol{B}_n) \tag{7}$$

Dynamics Model

ARTMS propagates the absolute orbits of observer and target spacecraft using fourth-order Runge-Kutta integration of the Gauss Variational Equations (GVE). For state $\boldsymbol{\alpha}$, the osculating OE of each spacecraft evolve according to

$$\dot{\boldsymbol{\alpha}} = G(\boldsymbol{\alpha})\boldsymbol{d}^{\mathcal{R}} \tag{8}$$

4

where $G \in \mathbf{R}^{6 \times 3}$ is the well-documented GVE state transition matrix[23] and $\boldsymbol{d}^{\mathcal{R}}$ is the perturbing acceleration expressed in $\mathcal{R}$. In GEO, perturbations caused by J_2 gravity, SRP and third-body gravity are of similar significance.[24] Analytic models have been developed for the effects of J_2 and third-body gravity on the mean OE,[25,26] as have analytic models for the effects of J_2 and SRP on the ROE.[21,27] Spacecraft ballistic coefficients are dynamically modeled as constants within ARTMS.

A useful aspect of the ROE is that they provide geometric intuition regarding target relative motion. As initially shown by D'Amico[20] for near-circular orbits, there is a linear map between the ROE and the target's curvilinear position vector $\delta \boldsymbol{r}$ in the observer's RTN frame. This was extended to eccentric orbits[22] by defining the eccentric ROE $\delta \boldsymbol{\alpha}^* = (\delta a, \delta \lambda^*, \delta e_x^*, \delta e_y^*, \delta i_x, \delta i_y)$, which revert to traditional ROE for $e_o \approx 0$. The resulting mapping is

$$\delta \boldsymbol{r}^{\mathcal{R}} = \begin{bmatrix} \delta r_R \\ \delta r_T \\ \delta r_N \end{bmatrix} \approx r_o \begin{bmatrix} \delta a - \frac{e_o}{2} \delta e_x^* - \delta e^* \left(\cos(\nu_o - \phi^*) + \frac{e_o}{2} \cos(2\nu_o - \phi^*) \right) \\ \delta \lambda^* + \delta e^* \left(2 \, \sin(\nu_o - \phi^*) + \frac{e_o}{2} \, \sin(2\nu_o - \phi^*) \right) \\ \delta i \sin \left(\nu_o + \omega_o - \theta \right) \end{bmatrix} \tag{9}$$

where r is orbit radius, ν is true anomaly, and $\theta = \omega + \nu$ is true longitude. Subsequently, a second-order mapping for eccentric orbits was developed,[28] expressed as

$$\delta \boldsymbol{r}^{\mathcal{R}} = \begin{bmatrix} \delta r_R \\ \delta r_T \\ \delta r_N \end{bmatrix} = r_o \begin{bmatrix} \boldsymbol{b}_R(\theta_o)\delta \boldsymbol{\alpha} + \delta \boldsymbol{\alpha}^\top B_R(\theta_o)\delta \boldsymbol{\alpha} \\ \boldsymbol{b}_T(\theta_o)\delta \boldsymbol{\alpha} + \delta \boldsymbol{\alpha}^\top B_T(\theta_o)\delta \boldsymbol{\alpha} \\ \boldsymbol{b}_N(\theta_o)\delta \boldsymbol{\alpha} + \delta \boldsymbol{\alpha}^\top B_N(\theta_o)\delta \boldsymbol{\alpha} \end{bmatrix} \tag{10}$$

where $\boldsymbol{b}_i \in \mathbb{R}^6$ are vectors containing the time-varying coefficients of the first-order mapping and $B_i \in \mathbb{R}^{6 \times 6}$ are triangular matrices containing the time-varying coefficients of the second-order terms. Terms in $\boldsymbol{b}_i$ and B_i are fully defined by Willis.[28]

Figure 2 presents relative motion in $\mathcal{R}$ for small separations. Oscillatory motion produced by target relative orbits is shown in black, possessing the same frequency as the orbit. Oscillatory motion produced by orbit eccentricity is shown in red, acting at twice the frequency of the orbit. δa and $\delta \lambda^*$ capture mean offsets in the radial and along-track directions respectively; magnitudes of δe^* and δi correspond to magnitudes of oscillations in the RT and RN planes respectively; and phases of δe^* and δi dictate the orientation and aspect ratio of the tilted ellipse in the RN plane. The eccentricity of the observer's orbit superimposes additional offsets and higher-frequency oscillations in the RT and RN planes.

ARTMS NAVIGATION ARCHITECTURE

ARTMS is a self-contained navigation architecture that provides autonomous, distributed angles-only navigation for multi-agent space systems.[13] The following terminologies are adopted. "Observer" refers to the spacecraft hosting the instance of ARTMS being discussed. A "remote observer" is another spacecraft hosting ARTMS that is providing measurements over the inter-satellite link (ISL). The "system" consists of all observers and all other relevant "targets", which are space objects tracked by observers. Each observer might only track a subset of the system and targets may themselves be remote observers. Figure 3 presents an example (not to scale).

A high-level overview of ARTMS is presented in Figure 4. It consists of three core software modules: IMage Processing (IMP),[14] Batch Orbit Determination (BOD)[15] and Sequential Orbit Determination (SOD).[12] Data sources are the VBS, which provides time-tagged images to ARTMS; the ISL, which communicates orbit estimates and bearing angle measurements between observers; and the ground segment, which provides telecommands and maneuver plans. In this paper, it is assumed GNSS measurements are unavailable.

The operation of each module is briefly described as follows. First, the IMP module uses VBS images to produce batches of bearing angle measurements with corresponding uncertainties for all detected targets in the FOV. The only prior information needed by IMP is a coarse estimate of the observer's absolute orbit at a single past epoch. Sample times for IMP images are typically 0.5-5% of the orbit period. The BOD module
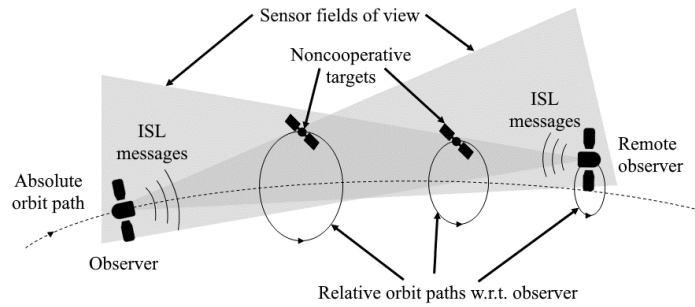
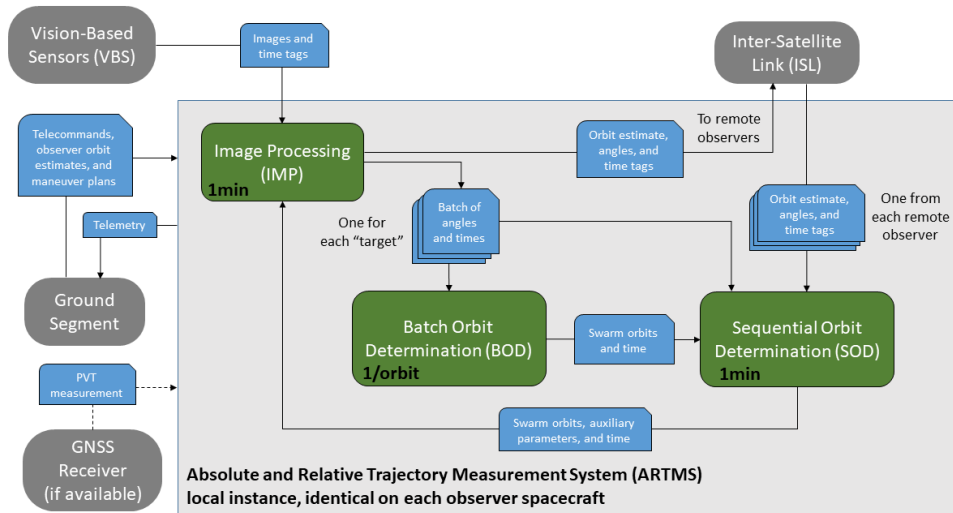**Figure 3**: Illustration of ARTMS observers and targets. Not to scale.

Figure 4: General architecture of ARTMS including external systems/data sources (dark gray), software modules (green), and exchanged data (blue). GNSS inputs (when available) and ground inputs are provided to all modules. Ground telemetry consists of all module outputs.

uses IMP angle batches, and the aforementioned observer orbit estimate, to compute state estimates for the observer and its targets. BOD is run once per orbit. The SOD module uses the BOD estimate to initialize a UKF, which fuses measurements from IMP and remote observers to refine the state estimates of the observer and its targets. Use of multiple observers for distributed stereo vision greatly improves state observability. SOD then provides updated state estimates to IMP to more efficiently assign new bearing angles to targets. The SOD orbit estimate and IMP bearing angles are sent to the ISL, and subsequent BOD estimates are used for fault detection in SOD and re-initializations in contingency cases. All modules may utilize ground information when appropriate such as knowledge of planned maneuvers.

In this fashion, ARTMS is distributed and scalable to arbitrary system sizes. Furthermore, modules require almost no contact with ground-based resources. Novel algorithms self-initialize navigation using a single external absolute orbit measurement per observer and modules take advantage of additional information when available to enable autonomy. IMP, BOD and SOD algorithms are described in more detail in the following, along with extensions to support navigation in GEO.

6

Image Processing

The objective of IMP is to produce batches of time-tagged bearing angle measurements to each target using a coarse estimate of the observer's orbit and images provided by the VBS.

First, a centroiding algorithm is used to simplify the image into a list of pixel cluster centroids.[29] Centroids are converted to unit vectors in the VBS frame using a calibrated camera model. Next, the Pyramid star identification algorithm[30] is applied to remove stellar objects (SO) from the list of vectors. Uncatalogued SO are detected as objects with unchanging inertial unit vectors between images and camera hotspots are detected as objects with unchanging pixel coordinates.[11] The VBS attitude is computed from the pointing vectors to identified stars in the inertial and sensor frames using the q-method.[31] The remaining minimal set of inertial unit vectors corresponds to potential targets and other unknown objects. An example image is provided in Figure 5.
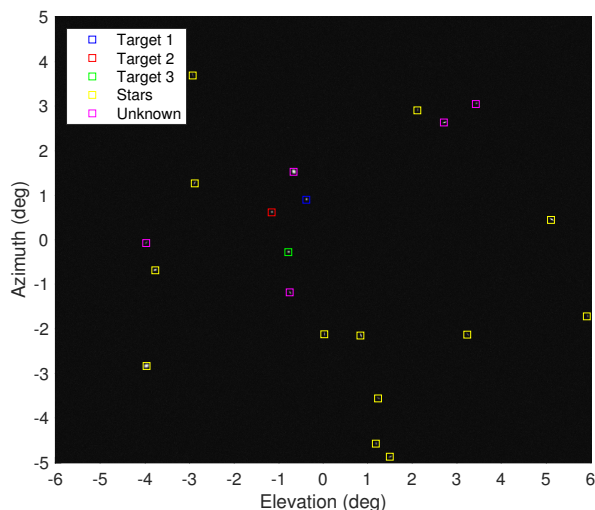

Figure 5: Example input image with point sources detected and identified by IMP as either target spacecraft, stars, or unknown RSO.[12]

If SOD is initialized, IMP applies single-hypothesis tracking. The SOD state estimate is used to compute modeled bearing angles (α_m, ϵ_m) and associated covariance region $\Sigma_m \in \mathbb{R}^{2 \times 2}$ for each target via an unscented transform. Subsequently, the Mahalanobis distance σ_m between modeled and measured angles is used to assign measurements to known targets, with

$$\sigma_m = \sqrt{(\alpha - \alpha_m, \epsilon - \epsilon_m)\Sigma_m^{-1}(\alpha - \alpha_m, \epsilon - \epsilon_m)^\top} \tag{11}$$

Let σ_{ij} denote the Mahalanobis distance between the i'th unidentified measurement and the modeled measurement of the j'th tracked target. To minimize erroneous assignments, the i'th measurement from the remote observer is assigned to the j'th target if three conditions are satisfied:

$$1)\ \sigma_{ij} \leq \sigma_{\max} \qquad 2)\ \frac{\sigma_{ij}}{\min\limits_{k \neq i} \sigma_{kj}} \leq \sigma_{\text{meas}} \qquad 3)\ \frac{\sigma_{ij}}{\min\limits_{l \neq j} \sigma_{il}} \leq \sigma_{\text{model}} \tag{12}$$

These conditions ensure 1) measurement i is close to modeled measurement j; 2) measurement i is closer to modeled measurement j than all other measurements; and 3) modeled measurement j is closer to i than all other targets. This paper applies $\sigma_{\max} = \sigma_{\text{meas}} = \sigma_{\text{model}} = 3$.

If no a-priori relative orbit knowledge is available, IMP applies multi-hypothesis tracking (MHT), and uses the novel Spacecraft Angles-only MUltitarget tracking System (SAMUS) algorithm to detect target tracks in sets of unidentified measurements.[14] SAMUS applies concepts of MHT[32] in that as measurements arrive, several simultaneous hypotheses are maintained for their association into target tracks. MHT robustly converges towards the correct hypothesis over time as more information becomes available by gating, scoring, and pruning propagated hypotheses. SAMUS achieves improved precision and efficiency compared to naive MHT by leveraging domain-specific knowledge to develop new kinematic scoring and trimming criteria. These criteria are derived from Equation 9, which maps OE and ROE to target relative position in $\mathcal{R}$. In Equation 9, the only quickly-varying terms are those which are functions of ν, whereas others vary slowly in the presence of perturbations[20] and are effectively constant on the timescales of image-to-image tracking. Target motion is therefore periodic with known form and even if specific ROE are unknown, this kinematic model can be leveraged to assess target tracks formed by successive measured unit vectors in $\mathcal{R}$.

The radial and cross-track components of Equation 9 can be fitted to track measurements and used to assess track quality and predict upcoming measurements. Applying the first-order model to measured bearing angles (α, ϵ) gives

$$\begin{bmatrix} \epsilon \\ \alpha \end{bmatrix}^{\mathcal{R}} \approx \frac{r_o}{a_o} \begin{bmatrix} x_1 - x_2(\cos(\nu_o - x_3) + \frac{e_o}{2}\cos(2\nu_o - x_3)) \\ x_4 + x_5\sin(\nu_o + \omega - x_6) \end{bmatrix} \tag{13}$$

where $x_{1,\ldots,6}$ are scaled ROE equivalents in bearing angle space and r, a, ν, e, ω are provided by the absolute orbit estimate. Thus, given at least three track measurements, $x_{1,\ldots,6}$ can be solved for via least squares. Kinematic rules are then derived from Equation 9 to gate which hypotheses are physically reasonable. Briefly, 1) track velocities must be below a set maximum, 2) track velocities must be consistent over time, 3) tracks should generally not feature acute angles, 4) tracks should turn in a consistent direction, and 5) new data must be close to the predicted measurement. Only tracks which pass all rules are propagated, and tracks are subsequently scored on how well they match expected kinematic behavior. Known target maneuvers can be assigned to tracks by matching qualitative similarities between changes in $x_{1,\ldots,6}$ pre- and post-maneuver to expected changes in the ROE from a state transition matrix.[33]

Image Processing Extensions

In the context of IMP, two difficulties are presented by GEO inspection and servicing. First, a-priori state information may possess position uncertainties on the order of tens of kilometers (3σ). Measurement assignment using fixed ambiguity thresholds becomes inconsistent or impossible, especially if targets are in proximity in the FOV. Large magnitudes of relative motion during rendezvous may also violate standard kinematic gating thresholds; however, if thresholds are relaxed, the hypothesis search space grows too large to be feasibly managed.

In response, a new hybrid tracking mode is introduced, in which SOD targets are allowed to become associated with multiple track hypotheses. First, bearing angle uncertainty regions from SOD are used as additional track gating criteria, to reduce the search space when kinematic rules are relaxed. Then, kinematic scoring over longer time periods is used to augment Mahalanobis-distance-based assignment metrics, to increase robustness when state information is highly uncertain. At each timestep, assigned measurements from the best hypothesis are passed to the filter. To prevent rapid switching between hypotheses, a measurement is only passed to SOD if its hypothesis branch has been the best-scoring for at least n_1 images, and its score is better than the second-best by a factor of at least n_2. This paper applies $n_1 = 3$ and $n_2 = 2$. In this fashion, SOD/SAMUS consensus is used to aid performance. Figure 6 presents the sequence of operations for IMP tracking modes.

The second difficulty arises from rendezvous scenarios in which multiple targets (e.g. a refueling depot and its customers) are in visual proximity. Their point spread functions (PSF) in images may merge, leading to inaccurate, ambiguous or missing target measurements. Given the high sensitivity of angles-only navigation to measurement errors[34] it is vital to detect and manage such events.
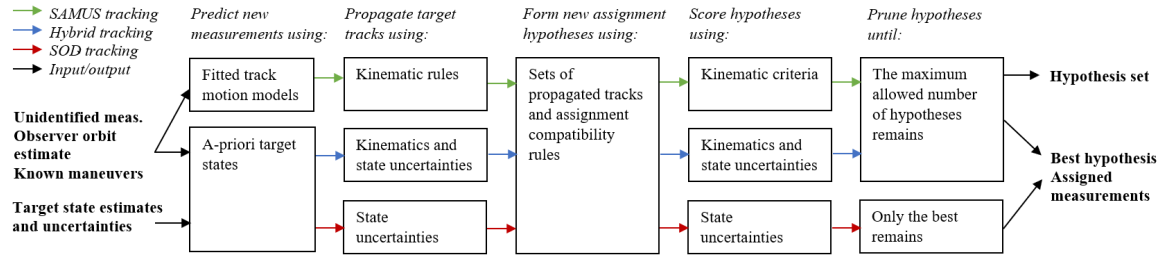
Figure 6: SAMUS algorithm sequence of operations.

Consider d_{ij}, the distance between modeled measurements for targets i and j. Define θ_{join}, an angular distance below which PSF are likely to partially merge, and θ_{same}, an angular distance below which PSF are likely to completely overlap. The following conditions are applied:

1. If $d_{ij} \geq \theta_{\text{join}} \ \forall \ j \neq i$, proceed with normal measurement assignment.
2. If $d_{ij} \leq \theta_{\text{same}}$, assign the same measurement to i and j (if one is suitable).
3. If $\theta_{\text{same}} < d_{ij} < \theta_{\text{join}}$, do not assign a measurement to i or j.

Thresholds are specified based on camera properties and expected target angular sizes with $\theta_{\text{join}} > \theta_{\text{same}}$. This paper applies $\theta_{\text{join}} = 500''$ and $\theta_{\text{same}} = 100''$. Figure 7 illustrates the three conditions.
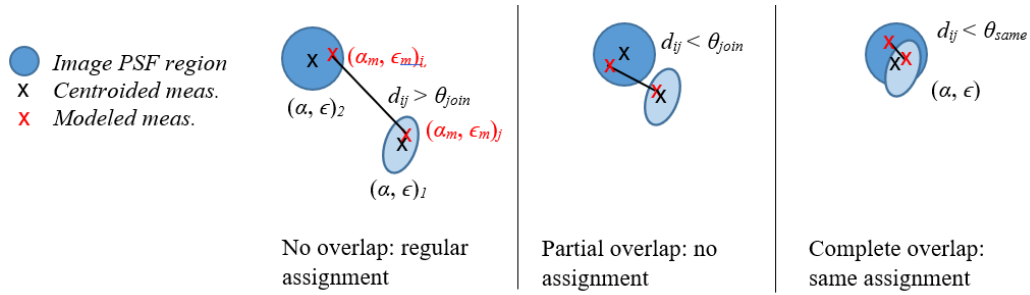

Figure 7: Example measurement assignment scenarios for targets i and j.

Batch Orbit Determination

The BOD module must produce orbit estimates for the system with sufficient accuracy to initialize the SOD module, using only a single coarse estimate of the observer orbit and batches of bearing angles to each target from the onboard VBS. State estimation is accomplished using a new algorithm[15] that applies the following procedure for each target.

First, a 1-D family of state estimates is computed for specified samples of $\delta\lambda$ using iterative batch least squares refinement, where the refined state consists of target ROE and the observer semimajor axis. Usage of this sampling approach is informed by a system observability analysis: in swarms and formation-flying scenarios, there is the underlying assumption of a weakly observable mode in mean along-track separation,[12] whereas for more general configurations (e.g. constellations) this is not always the case. A typical choice is to divide the expected state space for $\delta\lambda$ into 100-200 intervals in the positive and negative directions. It is important to minimize computation costs of sampling and thus, the analytic dynamics models described previously are used when propagating the refined state to each measurement epoch.

Second, the output state estimate is chosen as that which produces the least measurement residuals. The measurement noise matrix for each measurement (denoted $\boldsymbol{R}_{\text{vbs}}$) is then estimated using the measurement

residuals corresponding to the output state estimate. A conceptual illustration for a single target is shown in Figure 8.
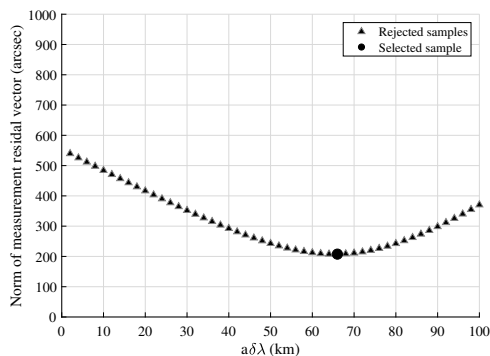

Figure 8: Conceptual illustration of converged BOD measurement residuals for rejected versus selected state estimates for specified $\delta\lambda$ values.
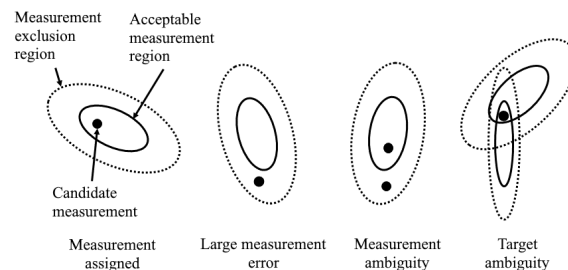

Figure 9: Illustration of conditions in which SOD measurement assignment criteria are satisfied (leftmost figure) and conditions that violate measurement assignment criteria (others).

Finally, the covariance for estimated state components $\boldsymbol{P}_{\text{est}}$ is computed via

$$\boldsymbol{P}_{\text{est}} = \boldsymbol{S}_{\text{est}}^{*}(\boldsymbol{R}_{\text{vbs}} + \boldsymbol{S}_{\text{prior}}\boldsymbol{P}_{\text{prior}}\boldsymbol{S}_{\text{prior}}^{T})\boldsymbol{S}_{\text{est}}^{*T} \tag{14}$$

where $\boldsymbol{S}_{\text{est}}^{*}$ is the pseudoinverse of the measurement sensitivity matrix for estimated state components, $\boldsymbol{S}_{\text{prior}}$ is the measurement sensitivity matrix for any a-priori state information, and $\boldsymbol{P}_{\text{prior}}$ is the uncertainty of a-priori state information. This formulation allows BOD to transition between domains where uncertainty is driven by sensor performance versus errors in the a-priori information.

Batch Orbit Determination Extensions

Typical measurement collection periods for BOD are 1-2 orbits of the observer, which is not always conducive to quickly evolving rendezvous scenarios. Furthermore, BOD applies linearized models for state estimation, which can lead to inaccuracies and poor convergence when ROE are large and e.g. the second-order effects of orbit curvature on measurements become apparent.

To address this, the use of fast initial relative orbit determination (IROD) methods is investigated as a potential complement to the existing BOD module. The method explored here is that of Willis,[28] which applies the second-order mapping from RTN position to the ROE presented in Equation 10. Given only three sets of bearing angles (and their corresponding unit vectors in $\mathcal{R}$), IROD can be performed for a target of interest by solving the resulting polynomial system of equations for the ROE. Willis also describes the 'INSPEQTER' algorithm as a suitable solver, which leverages domain-specific solution properties to compute solutions in a highly efficient manner.

This method has only been applied in literature to scenarios using Keplerian dynamics without Gaussian measurement noise, and its performance has not yet been quantified in the presence of more realistic noise and dynamics models. In addition, it does not natively provide an accompanying state uncertainty or indication of solution quality. Consequently, this paper proposes a sampling approach in which input angles are sampled from expected Gaussian error distributions around each true measurement, producing a set of output state samples which can be transformed into an IROD mean and covariance. This process is illustrated in Figure 10. Sampling may be performed via an unscented transform or in a Monte Carlo sense. When applying the unscented transform, the three input measurements are concatenated into a mean vector $\boldsymbol{y} \in \mathbb{R}^6$, with an associated diagonal covariance matrix $\boldsymbol{Y} \in \mathbb{R}^{6\times6}$ dependent on sensor noise properties, to generate 13 sigma points.
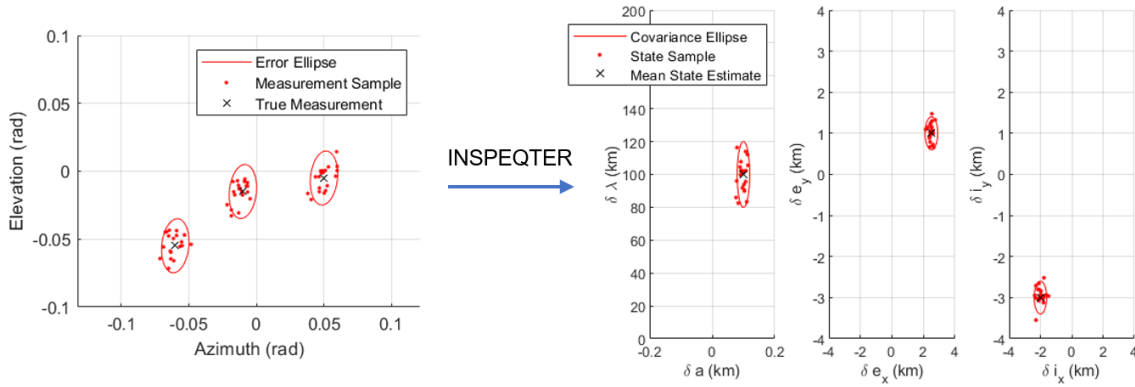
Figure 10: Conceptual illustration of measurement error sampling (left) to generate initial ROE covariances via INSPEQTER (right). Covariances are not to scale.

Sequential Orbit Determination

The SOD module continually refines orbit estimates and auxiliary state estimates of the observer and its targets by seamlessly fusing measurements from all observers transmitted over the ISL. SOD applies the bearing angle measurement model and numerical GVE dynamics model introduced earlier within a UKF framework. The choice of a UKF with an OE and ROE state parametrization provides crucial advantages. First, the weakly observable range to each target is primarily captured by $\delta\lambda$ in most relative motion geometries, with other ROE being strongly observable.[22] This allows ARTMS to maximize accuracy by applying separate state estimation techniques to different components (as seen in BOD). Second, the UKF is able to incorporate nonlinearities in the dynamics and measurement models and preserves higher-order moments in the probability distribution, to enable angles-only observer and target state convergence without maneuvers. Third, OE and ROE states vary slowly with time, which allows accurate numerical integration of the GVE with large timesteps for efficient onboard orbit propagation.

Three additional features maximize performance. First, adaptive process noise estimation is used to improve convergence speed and robustness to errors in the dynamics model.[12] Second, the state definition is organized to exploit the structure of the Cholesky factorization, reducing calls to the orbit propagator by almost a factor of two.[35] Third, measurements from remote observers are assigned to local targets for distributed stereo-vision. The observability of target relative states is greatly improved when multi-observer measurement sharing is active, and furthermore, if the observer-target system meets certain criteria,[9,36] the absolute orbits of system members become observable with only bearing angles. However, care must be taken to prevent the ambiguities of assigning multiple measurements to the same target or assigning the same measurement to multiple targets. Selection criteria are developed based on Mahalanobis distance thresholds to a) match orbit estimates broadcast by remote observers to local orbit estimates of targets, and b) match modeled bearing angles of local targets to measured bearing angles broadcast by remote observers.[18] Unambiguous correspondence must be achieved such that only one choice lies within a Mahalanobis assignment region and no other choices lie within a Mahalanobis exclusion region. Figure 9 provides a conceptual example for b).

Sequential Orbit Determination Extensions

GEO scenarios present further challenges that must be addressed by the SOD module. First is that RSO orbits are typically very close to equatorial, and operate near the zero-inclination singularity present in Keplerian or quasi-nonsingular orbit parametrizations. To avoid numerical instability in the UKF, ARTMS is extended to include the fully nonsingular OE and ROE states previously defined, and implements the relevant GVE matrices, state transition models and state conversions.

Furthermore, SRP forces may have significant perturbative effects on observer and target orbits, especially

over longer time periods. However, the values of SRP ballistic coefficients may not necessarily be well-known (especially for non-cooperative targets) and may vary over time. Incorrect values provided to the filter a-priori will cause biases or divergences in estimated ROE. To eliminate these errors and improve filter robustness, ballistic coefficients are instead estimated online within ARTMS. Within the UKF, B_{srp} and δB_{srp} values are appended to the system state vector, and are included when generating sigma points for prediction and update steps. When each sigma point orbit is later propagated, the numeric integration applies the corresponding sigma point ballistic coefficient value. Observability of ballistic coefficients is verified via simulation.

SIMULATION SCENARIOS

Five simulation scenarios are developed to demonstrate autonomous angles-only navigation for multiple agents in GEO. Initial conditions are given in Tables 1 and 2. Absolute orbits are specified for a 'chief' observer and relative orbits are specified with respect to this observer.

Scenarios A and B present a rendezvous approach by a single observer spacecraft (S/C) towards a target of interest, with two additional targets in the FOV. Scenario A considers a high-thrust maneuver over two hours, whereas Scenario B considers a low-thrust maneuver over one day. Applications include servicing, inspection or refueling of targets in GEO.

Scenarios C and D present detection and characterization of multiple target spacecraft by two cooperative observers. Scenario C considers targets whose orbit states are coarsely known a-priori, whereas Scenario D considers targets whose states are entirely unknown. Applications include inspection and tracking of cooperative or uncooperative GEO targets.

Scenario E presents a refueling scenario in which three smaller spacecraft dock and refuel at a mothership 'depot' in sequence over one day, via a series of pre-planned maneuver waypoints. It is assumed targets cooperate with the depot over an ISL but do not actively cooperate with each other.

Simulation conditions for each scenario are presented in Table 3. The frequency of camera measurements is modified depending on maneuver activity, and observers may actively or passively track targets with the onboard VBS. 'Active' tracking implies modifying attitude to approximately center known targets in the FOV, whereas 'passive' tracking implies consistent pointing of the VBS boresight in the (anti-)velocity direction. Active tracking is applied when relative motion is large. Target state estimates are either initialized via a-priori information from the ground, or autonomously on-board using BOD.

Maneuvers are executed in Scenarios A, B and E. In Scenario A, a maneuver with $\delta\boldsymbol{v} = [-5.28, 5.39, 0.52]$ m/s is performed at simulation time $t = 1$ hour with a burn time of 2 hours. In Scenario B, a maneuver with $\delta\boldsymbol{v} = [0, 0.18, 0]$ m/s is performed at $t = 10$ hours with a burn time of 20 hours. In Scenario E, each target spacecraft performs between 6-8 impulsive maneuvers during rendezvous, docking and departure from the depot. Relative orbits are plotted in Figure 11.

Table 1: Chief spacecraft initial states for simulations.

Scenario	Chief ID	a (km)	e	i (°)	Ω (°)	ω (°)	M_0 (°)	B_{srp}
A	1	42014	0.00015	0.01	97.8	67.7	307.9	0.025
B	1	42159	0.00015	0.01	97.8	67.7	307.9	0.025
C, D	1	42164	0.00015	0.01	0.0	0.0	0.0	0.025
E	1	42164	0.00015	0.01	0.0	0.0	0.0	0.015

Data Generation

Ground truth positions and velocities of all spacecraft are obtained by numerically integrating the GVE. Included perturbations are summarized in Table 4. Spacecraft are physically modeled as smallsats with a mass of 250 kg and constant sun-facing cross-sectional area of 2.5 m^2. The refueling depot is modeled as a larger bus with a mass of 5000 kg and cross-sectional area of 30 m^2. Target visibility and visual magnitudes
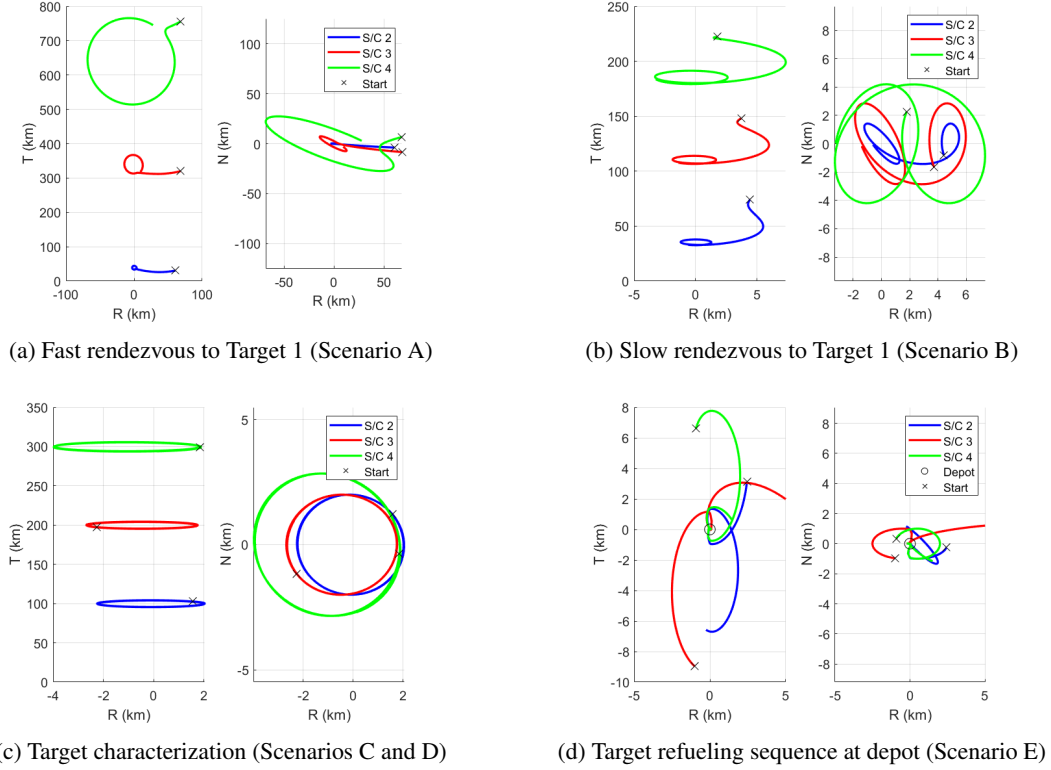
(a) Fast rendezvous to Target 1 (Scenario A)

(b) Slow rendezvous to Target 1 (Scenario B)

(c) Target characterization (Scenarios C and D)

(d) Target refueling sequence at depot (Scenario E)

Figure 11: Relative positions of targets with respect to S/C 1 (the origin) in the RT and RN planes.

Table 2: Deputy spacecraft initial states for simulations.

Scenario	Deputy IDs	$a\delta a$ (km)	$a\delta\lambda$ (km)	$a\delta e_x$ (km)	$a\delta e_y$ (km)	$a\delta i_x$ (km)	$a\delta i_y$ (km)	δB_{srp}
A	2, 3, 4	150, 150, 150	300, 600, 900	60, 60, 30	150, 150, 100	5, 10, -15	5, 10, -15	0
B	2, 3, 4	5, 5, 5	75, 150, 225	0.5, 1, 2	0.5, 1, 2	1, 2, -3	1, 2, -3	0
C	2, 3, 4	0, 0, 0	100, 200, 300	0, 0, 2	2, -2, 2	0, 0, 2	2, -2, 2	0
D	2, 3, 4	0, 0, 0	100, 200, 300	0, 0, 2	2, -2, 2	0, 0, 2	2, -2, 2	0
E	2, 3, 4	0.5, -0.5, 0.5	4.1, -5.1, 5.6	-1.9, 0.6, 1.4	0.5, 1.9, -0.5	-1, 0.3, 0.9	0.3, 1, -0.2	0

are computed using a model which takes into account the observer-target-Sun phase angle and variations in reflected flux from different satellite surfaces.[37] Eclipse and camera blinding periods are also modeled.

Measurements are synthesized from the ground truth with injected Gaussian noise as per Table 4. VBS images are generated using 3D vector graphics in OpenGL.[38] Visual magnitudes, angles, and proper motions of stars are obtained from the Hipparcos star catalog and objects within the camera FOV (including RSO) are rendered using Gaussian PSF. Mismatches between known and true camera parameters are modeled by adding Gaussian noise to PSF positions and Gaussian noise is added to pixel intensities. Control errors for spacecraft attitude are also modeled, as are magnitude and direction errors for executed maneuvers. After injected errors, centroiding errors, and attitude determination errors, inertial bearing angle errors are approximately $15''$ (1σ). Future work will explore integration of spacecraft 3D models into imagery when operating at close range.

Inputs are processed by ARTMS in the form of a multi-satellite simulation in MATLAB Simulink and C++. Perturbations modeled within SOD are summarized in Table 4, and errors in a-priori target state information are summarized in Table 3. BOD initialization occurs after 24 hours when used. Adaptive process noise estimation is applied in SOD and empirical accelerations are not estimated.

Table 3: Summary of simulation conditions.

Scenario	Observer IDs	Simulation Length	Attitude	Number of Maneuvers	Maneuver Duration	IMP Meas. Frequency	SOD Dyn. Step Size	Initialization Method	A-priori State Error (3σ) Position	B_{srp}
A	1	10 hrs	Active	1	2 hrs	300 s	150 s	Ground	10 km	30%
B	1	50 hrs	Active	1	20 hrs	1200 s	600 s	Ground	10 km	30%
C	1, 4	150 hrs	Passive	-	-	1200 s	600 s	Ground	3 km	30%
D	1, 4	150 hrs	Passive	-	-	1200 s	600 s	BOD	3 km	30%
E	1, 4	25 hrs	Active	22	1 sec	300 s	150 s	Ground	50 m	30%

Table 4: Dynamics models and measurement noise for simulations.

Model	Perturbations	Propagation	Measurement	Noise (1σ)	Axes
IMP	Keplerian (none)	Analytic	Image pixel intensity	1.5%	-
BOD	J_2 gravity	Analytic	Image PSF position	$[5, 5]''$	$[\alpha, \epsilon]$
SOD	5x5 GRACE gravity model Solar radiation pressure with cannonball drag model Third-body lunisolar gravity	RK4 integrator 150-600 s timestep	Attitude control	$[10, 10, 30]''$	$[\hat{\boldsymbol{x}}^{\mathcal{V}}, \hat{\boldsymbol{y}}^{\mathcal{V}}, \hat{\boldsymbol{z}}^{\mathcal{V}}]$
Truth	60x60 GRACE gravity model Solar radiation pressure with cannonball drag model Third-body lunisolar gravity	RK4 integrator 10 s timestep	Maneuver magnitude Maneuver direction	2% $[2, 2, 2]°$	- $[\hat{\boldsymbol{x}}^{\mathcal{R}}, \hat{\boldsymbol{y}}^{\mathcal{R}}, \hat{\boldsymbol{z}}^{\mathcal{R}}]$

Simulation Results

Figure 12 presents relative navigation results for Scenario A, where time $t = 0$ corresponds to the initialization of SOD. Steady-state estimation performance is given in Table 5. The majority of position error occurs in the along-track direction which is analogous to the weakly observable target range. Other components of target motion are more observable and see correspondingly smaller errors. Despite large initial position uncertainties of $[10, 10, 10]$ km (3σ) in the $[\hat{\boldsymbol{x}}^{\mathcal{I}}, \hat{\boldsymbol{y}}^{\mathcal{I}}, \hat{\boldsymbol{z}}^{\mathcal{I}}]$ axes, tracking is robustly established and uncertainties are reduced to ~1 km in target position by commencement of the maneuver. Targets are successfully tracked throughout the maneuver period despite the presence of associated errors, with final state uncertainty on the order of several hundred meters or 0.1% of target range. It was observed that estimation of δB_{srp} coefficients during maneuvers causes some instability, because the filter is unable to distinguish between dynamical changes caused by maneuver execution errors or ballistic coefficient errors. It is therefore recommended to de-couple maneuver updates and B_{srp} estimation.
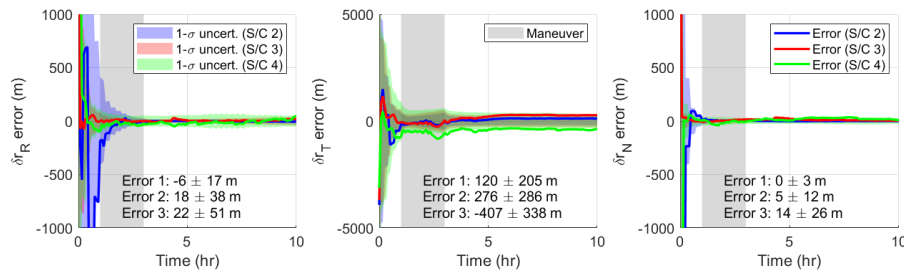
Figure 12: Relative position errors and uncertainties in the RTN frame for S/C 1 (Scenario A).

As intersatellite range increases, the noise floor of the VBS corresponds to larger state uncertainties. Thus, angles-only state uncertainties are somewhat proportional to range, and state uncertainties in Scenario B are comparatively larger than in Scenario A. This is primarily due to the longer simulation period during which the observer does not receive any external absolute orbit updates. In the case of angles-only measurements, a single observer can only fully observe relative orbit states, whereas multi-observer measurement sharing is

Table 5: Mean state error and 1σ state uncertainty at the end of the simulation period, for ARTMS running on board S/C 1.

Scenario	S/C ID	r_R (m)	r_T (m)	r_N (m)	v_R (mm/s)	v_T (mm/s)	v_N (mm/s)	B_{srp}
C	1	-28 ± 38	-393 ± 1554	138 ± 140	1 ± 3	4 ± 4	-35 ± 33	-
D	1	263 ± 263	-759 ± 1894	11 ± 195	-8 ± 33	-38 ± 38	-14 ± 20	-
E	1	-4 ± 323	107 ± 1751	-4 ± 30	1 ± 5	0 ± 38	-1 ± 15	-

		δr_R (m)	δr_T (m)	δr_N (m)	δv_R (mm/s)	δv_T (mm/s)	δv_N (mm/s)	δB_{srp}
A	2	-6 ± 17	120 ± 205	0 ± 3	0 ± 3	1 ± 4	0 ± 1	-
	3	18 ± 38	276 ± 286	5 ± 12	2 ± 6	-2 ± 6	-1 ± 1	-
	4	22 ± 51	-407 ± 338	14 ± 26	6 ± 10	-2 ± 8	-2 ± 2	-
B	2	-1 ± 15	80 ± 175	-1 ± 3	-1 ± 3	0 ± 2	0 ± 1	-
	3	0 ± 50	-33 ± 463	-2 ± 6	0 ± 4	0 ± 6	0 ± 1	-
	4	-6 ± 88	19 ± 741	1 ± 8	0 ± 3	1 ± 10	0 ± 1	-
C	2	-1 ± 6	60 ± 138	1 ± 2	0 ± 1	0 ± 1	0 ± 1	$3 \times 10^{-5} \pm 3 \times 10^{-4}$
	3	-3 ± 7	58 ± 253	2 ± 3	0 ± 1	0 ± 1	0 ± 1	$-2 \times 10^{-5} \pm 4 \times 10^{-4}$
	4	-5 ± 14	71 ± 359	3 ± 4	0 ± 1	1 ± 1	0 ± 1	$-7 \times 10^{-5} \pm 4 \times 10^{-4}$
D	2	2 ± 6	234 ± 525	-3 ± 7	0 ± 1	0 ± 1	0 ± 1	$-6 \times 10^{-6} \pm 1 \times 10^{-4}$
	3	-7 ± 16	472 ± 1065	4 ± 8	0 ± 1	1 ± 2	0 ± 1	$7 \times 10^{-6} \pm 3 \times 10^{-4}$
	4	-7 ± 15	662 ± 1510	-5 ± 14	-1 ± 1	0 ± 1	0 ± 1	$-4 \times 10^{-6} \pm 4 \times 10^{-4}$
E	2	0 ± 2	-2 ± 9	0 ± 2	0 ± 1	0 ± 1	0 ± 0	-
	3	-1 ± 22	2 ± 36	0 ± 2	0 ± 1	0 ± 3	0 ± 1	-
	4	0 ± 2	0 ± 2	0 ± 1	0 ± 1	0 ± 1	0 ± 1	-

required for absolute orbit observability.[9,36] The observer's absolute orbit estimate therefore slowly diverges throughout the simulation which has detrimental effects on its relative orbit estimates also. However, the degradation is slow enough that (for example) a daily coarse absolute orbit update from the ground is sufficient to maintain strong navigation performance. Overall, the low-thrust maneuver is successfully tracked.

Figure 13 presents relative navigation results for Scenario D after an autonomous BOD initialization. The IMP module successfully tracks the three unknown targets in the field of view, and the BOD module is able to successfully generate initial relative state estimates from IMP measurement batches. Initial position uncertainties are on the order of 10 km, or 10-20% of target range. Comparatively, Scenario C results are significantly improved due to their reduced initial position uncertainty of 3 km. Augmentations to the BOD module are therefore proposed to enable more responsive and robust navigation, such as inclusion of analytic SRP dynamics models to reduce dynamics uncertainty, or the addition of multi-observer BOD for enhanced angles-only observability.

Convergence in Scenarios C and D is aided by multi-observer measurement sharing, which also allows estimation of the observers' absolute orbits for long-term autonomous navigation in GEO. Absolute orbit uncertainty is on the order of kilometers at steady state and may be further reduced by the addition of more observers to the system or by leveraging more distinct observer measurement baselines. Figure 13 demonstrates that the differential ballistic coefficients between the observer and each target are also observable using bearing angles, and can be estimated to reduce orbit state errors. The error spike at $t = 80$ hours in the r_T and δr_T estimates is due to an incorrect measurement assignment by IMP when an unidentified star crosses the FOV. Although the resulting state error is significant, it is soon recovered after new measurements from both observers.

State estimates for S/C 4 (the final spacecraft to refuel at the depot) are displayed in Figure 14 for Scenario E. State uncertainties are on the order of meters to tens of meters throughout, indicating that angles-only navigation can support safe rendezvous operations, if applied in concert with additional sensors to aid docking at very close ranges. Maneuver execution errors cause initial uncertainty increases, e.g. at $t = 6$ hours, but overall, maneuvers improve uncertainty over longer time periods by aiding disambiguation of target range. State uncertainties are also somewhat proportional to target range, as can be seen in the larger relative position
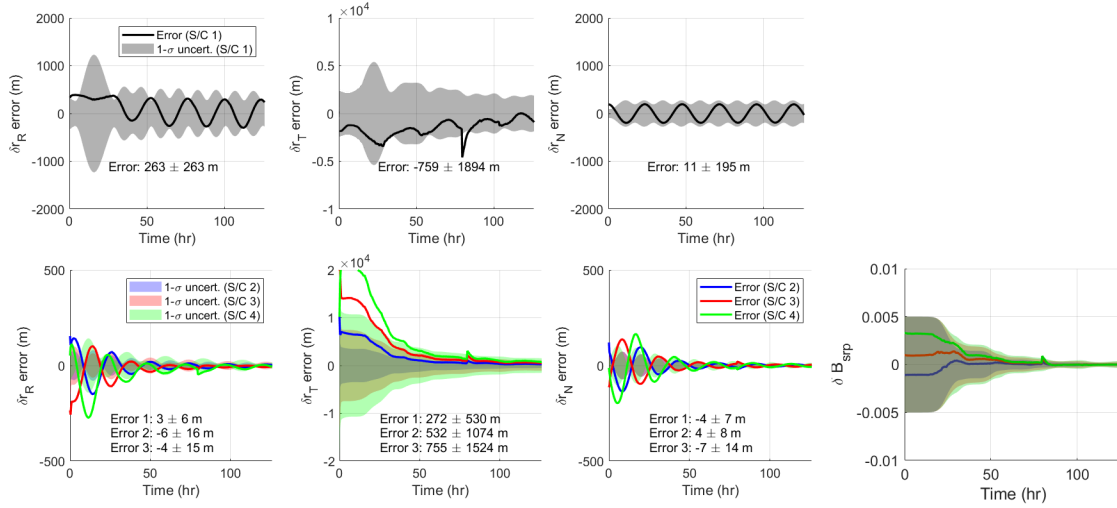
Figure 13: Absolute position (top), relative position (bottom) and δB_{srp} (right) errors and uncertainties in the RTN frame for S/C 1 (Scenario D).
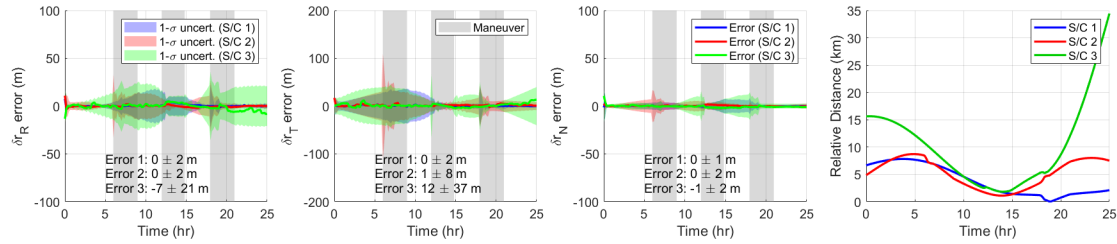

Figure 14: Relative position errors and uncertainties (left) and relative distances (right) in the RTN frame for S/C 4 (Scenario E). Maneuver blocks correspond to S/C 2, 3 and 4 as time advances.

uncertainty of S/C 3 towards the end of the simulation, as compared to the smaller uncertainties for S/C 1 (the depot).

Fast IROD Performance Analysis

In scenarios where responsive navigation is necessary, IROD estimates may be needed on shorter timescales than the full orbit required by the existing BOD algorithm. For example, in Scenario A, when initial states are highly uncertain, fast IROD may be used to more robustly identify targets in the few hours before maneuvers occur. In Scenario D, when initial states are unavailable, it may be used to provide range estimates for target tracks within IMP in a fast, computationally-efficient manner for added robustness.

Four cases are selected for investigation, derived from Scenarios A, C and E but without maneuvers. ROE1 applies $\delta\boldsymbol{\alpha}_{\mathrm{QNS}} = [150, 300, 60, 150, 5, 5]^{\top}$ km and features long target range with significant relative motion. ROE2 applies $\delta\boldsymbol{\alpha}_{\mathrm{QNS}} = [0, 100, 0, 2, 0, 2]^{\top}$ km and features medium range with little relative motion. ROE3 applies $\delta\boldsymbol{\alpha}_{\mathrm{QNS}} = [0.5, 4.1, -1.9, 0.5, -1, 0.3]^{\top}$ km and features short range with significant relative motion. Finally, ROE4 applies $\delta\boldsymbol{\alpha}_{\mathrm{QNS}} = [-5, 50, 100, 20, -100, 0]^{\top}$ km and features medium range with significant relative motion.

Three sampling methods for generating an IROD mean and covariance via the INSPEQTER algorithm are proposed. The first applies an unscented transform (UT) to generate sigma points from the true measurement set $\boldsymbol{y}$ and sensor noise covariance matrix $\boldsymbol{Y}$. The second uses Monte Carlo samples (MC1), drawn from a Gaussian distribution $\mathcal{N}(\boldsymbol{y}, \boldsymbol{Y})$. Solution quality for either method is dependent on the amount of measure-

ment error already present y (which serves as the mean about which samples are drawn). The third method (MC2) attempts to bypass this issue by instead performing Monte Carlo sampling in time. Consider a VBS taking images every $t_s = 10$ seconds, and denote t_m as the period between input measurements in y ,with $t_s \ll t_m$. Then, the first Monte Carlo sample is made up of images from times $\boldsymbol{t}_1 = [0, t_m, 2t_m]$ and the i'th sample is made up of images from times $\boldsymbol{t}_i = [(i-1)t_s, (i-1)t_s + t_m, (i-1)t_s + 2t_m]$. This paper assumes noise is uncorrelated between images such that measurement errors can be reduced via averaging, though some correlation may be present in practice. Note that it has been shown that the INSPEQTER method is able to remove constant biases from measurements, if present.[28]

Given that the shape and orientation of the relative motion ellipse is strongly observable, results quality is primarily distinguished by the estimation of weakly observable $\delta\lambda$. Indeed, a primary advantage of solving the second-order model of Equation 10 is that it provides a fixed $\delta\lambda$ solution, whereas the first-order model of Equation 9 does not. Thus, results are presented in the context of $\delta\lambda$, with the goal of achieving $\delta\lambda$ errors and uncertainties of less than 20% (approximately). Full-force dynamics are applied to all simulations.
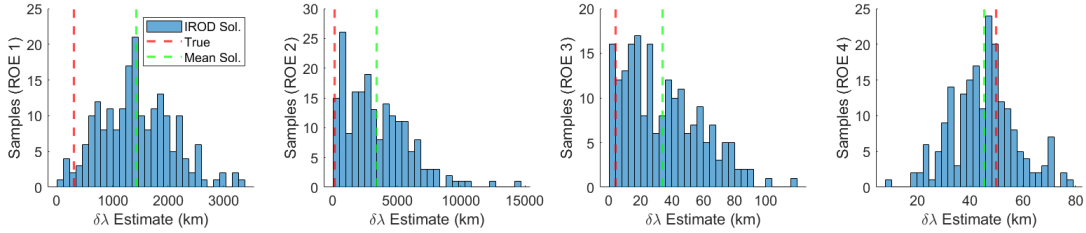

Figure 15: $\delta\lambda$ histograms for 200 Monte Carlo samples.
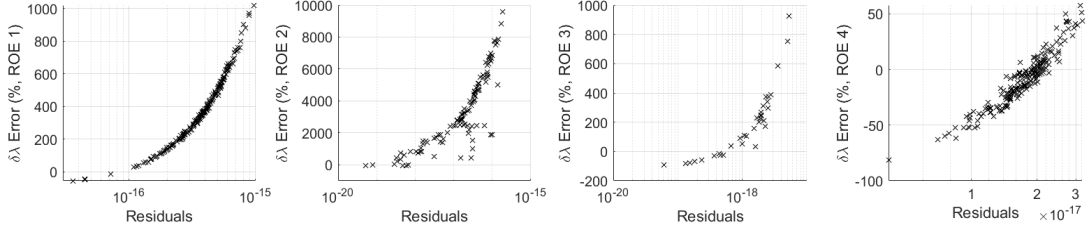

Figure 16: Scatter plots of solution residuals versus $\delta\lambda$ errors for 200 Monte Carlo samples. Note that not all residuals are visible in the center pair of plots, for readability.

Figure 15 presents histograms for output $\delta\lambda$ solutions across 200 samples, using $t_m = 1$ hr and 1σ bearing angle noise $\sigma_{\alpha,\epsilon} = [2, 2]''$. It is clear that for ROE1-3, the fast IROD method is very likely to vastly over-estimate $\delta\lambda$, leading to a poor mean output. However, solution quality is much improved for ROE4. This is due to the much larger δi for ROE 4 and resulting larger magnitude of out-of-plane motion, which significantly aids angles-only observability. Figure 16 presents solution residuals across the same 200 samples. Although smaller residuals are likely to correspond to smaller errors, there is also correspondence between magnitude of $\delta\lambda$ and magnitude of residuals, and the sample with the minimum residual is not necessarily best. Thus, residuals are not in themselves a final indication of solution quality.

Figure 17 presents trends in $\delta\lambda$ errors and uncertainties as $\sigma_{\alpha,\epsilon}$, t_m and δi are varied, for ROE1 and ROE4. Several trends are apparent. First, uncertainties are broadly similar between the UT, MC1 and MC2 sampling methods. However, the MC2 method tends to produce smaller errors, indicating that it is able to somewhat reduce the effects of measurement noise. Second, the expected behavior is generally observed, in that increasing noise decreases solution quality; increasing the measurement period increases solution quality (because the effects of noise become proportionally smaller compared to dynamical motion); and increasing δi increases solution quality and observability. Note that sampling is in some cases inordinately affected by very large outliers, and thus, it is recommended to perform 'sanity checks' to filter out unreasonable samples.

BOD typically produces initial ranges uncertainties of $<20\%$, and to achieve a similar quality with the fast IROD method while taking advantage of small t_m, low sensor noise of $\leq 2''$ is necessary. The most consistent results are obtained with sub-arcsecond accuracy, which may require specific telescope hardware to support initialization. Alternately, it may be possible to use coarser sensing with $2\text{-}5''$ accuracy if the orbit of the target tracking satellite is designed to be slightly above or below $i = 0$, thus possessing large δi compared to most GEO targets. The extreme sensitivity of the method to noise is expected due to the comparative lack of measurement information compared to BOD, which typically operates on 50-200 measurements. Furthermore, recall that the IROD dynamics model is Keplerian, and results are therefore affected by dynamics errors also. Future work will explore the addition of maneuvers and other dynamics to the model for increased generality.
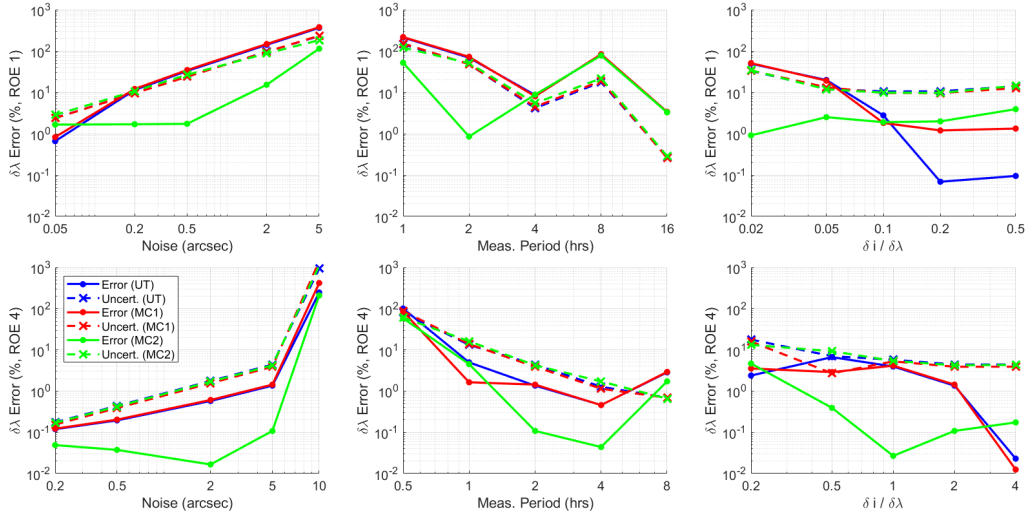

Figure 17: Solution $\delta\lambda$ error versus measurement noise, measurement period, and magnitude of the relative inclination vector for Cases 1 (top) and 4 (bottom).

CONCLUSION

This research presents an architecture for autonomous, distributed, angles-only navigation of multi-agent space systems in GEO, in support of satellite servicing and future space sustainability. The Absolute and Relative Trajectory Measurement System (ARTMS) consists of three core algorithms, each of which requires modifications to successfully operate in the GEO environment. The image processing algorithm is extended with new tracking modes for improved robustness in the presence of varying target separations and large state uncertainties. New batch orbit determination algorithms enable initial relative orbit determination with shorter measurement arcs. Sequential orbit determination algorithms are augmented with estimation of SRP ballistic coefficients.

ARTMS is verified via high-fidelity simulations of navigation in several target rendezvous and tracking scenarios, including approach maneuvers, characterization of multiple unknown targets, and close-range refueling. ARTMS is able to navigate during manuever periods and in the presence of large initial state uncertainties, and converged relative position estimates display uncertainties of $<0.5\%$ of target range. Observers are also able to detect and initialize navigation for previously unknown targets, and may share measurements to achieve angles-only absolute orbit estimation and autonomous long-term state convergence. SRP ballistic coefficients may also be estimated online for additional robustness. New angles-only initial relative orbit determination methods requiring only three measurements are investigated, and are shown to be suitable for fast target identification if sensor noise is small or relative orbits have large inclination differences. Overall, results display navigation performance suitable for supporting satellite inspection and servicing in GEO.

Future research areas include optimization of observer attitudes to ensure targets consistently remain in view when relative motion is large, treatment of unknown target maneuvers via uncertainty-aware filtering, and fusion of additional measurement sources such as inter-satellite ranging to provide increased accuracy and precision in relevant scenarios.

ACKNOWLEDGMENTS

REFERENCES

[1] M. Rathnasabapathy, D. Wood, F. Letizia, S. Lemmens, M. Jah, A. Schiller, C. Christensen, S. Potter, N. Khlystov, M. Soshkin, *et al.*, "Space sustainability rating: Designing a composite indicator to incentivise satellite operators to pursue long-term sustainability of the space environment," *International Astronautical Congress*, International Astronautical Federation, 2020.

[2] B. L. Benedict, "Rationale for need of in-orbit servicing capabilities for GEO spacecraft," *AIAA SPACE 2013 Conference and Exposition*, 2013, p. 5444.

[3] J. S. Hudson and D. Kolosa, "Versatile On-Orbit Servicing Mission Design in Geosynchronous Earth Orbit," *Journal of Spacecraft and Rockets*, Vol. 57, No. 4, 2020, pp. 844–850.

[4] X. q. Chen and J. Yu, "Optimal mission planning of GEO on-orbit refueling in mixed strategy," *Acta Astronautica*, Vol. 133, 2017, pp. 63–72.

[5] N. H. Barbara, S. Lizy-Destrez, P. Guardabasso, and D. Alary, "New GEO paradigm: Re-purposing satellite components from the GEO graveyard," *Acta Astronautica*, Vol. 173, 2020, pp. 155–163.

[6] C. Kaiser, F. Sjöberg, J. M. Delcura, and B. Eilertsen, "SMART-OLEV—An orbital life extension vehicle for servicing commercial spacecrafts in GEO," *Acta Astronautica*, Vol. 63, No. 1, 2008, pp. 400–410.

[7] D. C. Woffinden and D. K. Geller, "Observability Criteria for Angles-Only Navigation," *IEEE Transactions on Aerospace and Electronic Systems*, Vol. 45, No. 3, 2009, pp. 1194–1208.

[8] Y. Hu, I. Sharf, and L. Chen, "Distributed orbit determination and observability analysis for satellite constellations with angles-only measurements," *Automatica*, Vol. 129, 2021, p. 109626.

[9] J. Kruger and S. D'Amico, "Observability Analysis and Optimization for Angles-Only Navigation of Distributed Space Systems," *11th International Workshop on Satellite Constellations & Formation Flying*, 2022.

[10] S. D'Amico, J.-S. Ardaens, G. Gaias, H. Benninghoff, B. Schlepp, and J. L. Jørgensen, "Noncooperative Rendezvous Using Angles-Only Optical Navigation: System Design and Flight Results," *Journal of Guidance, Control, and Dynamics*, Vol. 36, No. 6, 2013, pp. 1576–1595.

[11] J.-S. Ardaens and G. Gaias, "Angles-Only Relative Orbit determination in Low Earth Orbit," *Advances in Space Research*, Vol. 61, No. 11, 2018, pp. 2740–2760.

[12] J. Sullivan, A. W. Koenig, J. Kruger, and S. D'Amico, "Generalized Angles-Only Navigation Architecture for Autonomous Distributed Space Systems," *Journal of Guidance, Control, and Dynamics*, Vol. 44, No. 6, 2021, pp. 1087–1105.

[13] A. W. Koenig, J. Kruger, J. Sullivan, and S. D'Amico, "ARTMS: Enabling Autonomous Distributed Angles-Only Orbit Estimation for Spacecraft Swarms," *2021 American Control Conference (ACC)*, IEEE, 2021, pp. 4282–4289.

[14] J. Kruger and S. D'Amico, "Autonomous angles-only multitarget tracking for spacecraft swarms," *Acta Astronautica*, Vol. 189, 2021, pp. 514–529.

[15] A. W. Koenig and S. D'Amico, "Observability-Aware Numerical Algorithm for Angles-Only Initial Relative Orbit Determination," *2020 AAS/AIAA Astrodynamics Specialist Conference*, Lake Tahoe, CA, 2020.

[16] H. Sanchez, D. McIntosh, H. Cannon, C. Pires, J. Sullivan, S. D'Amico, and B. O'Connor, "Starling-1: Swarm Technology Demonstration," *32nd Annual Small Satellite Conference*, Logan, UT, 2018.

[17] K. Iiyama, J. Kruger, and S. D'Amico, "Autonomous Distributed Angles-Only Navigation and Timekeeping in Lunar Orbit," *ION International Technical Meeting*, 2022.

[18] J. Kruger, K. Wallace, and S. Koenig, A. W.an d D'Amico, "Autonomous Angles-Only Navigation for Spacecraft Swarms around Planetary Bodies," *IEEE Aerospace Conference*, 2021.

[19] D. A. Vallado and W. D. McClain, *Fundamentals of Astrodynamics and Applications*. Hawthorne, California: Microcosm Press, 4 ed., 2013.

[20] S. D'Amico, *Autonomous Formation Flying in Low Earth Orbit*. PhD thesis, Delft University, 2010.

[21] A. W. Koenig, T. Guffanti, and S. D'Amico, "New State Transition Matrices for Relative Motion of Spacecraft Formations in Perturbed Orbits," *Journal of Guidance, Control, and Dynamics*, Vol. 40, No. 7, 2017, pp. 1749–1768.

[22] J. Sullivan and S. D'Amico, "Nonlinear Kalman Filtering for Improved Angles-Only Navigation Using Relative Orbital Elements," *Journal of Guidance, Control, and Dynamics*, Vol. 40, No. 9, 2017, pp. 2183–2200.

[23] K. T. Alfriend, ed., *Spacecraft Formation Flying: Dynamics, Control, and Navigation*. Butterworth-Heinemann/Elsevier, 2010.

[24] O. Montenbruck and E. Gill, *Satellite Orbits: Models, Methods and Applications*. Springer, 2012.

[25] D. Brouwer, "Solution of the problem of artificial satellite theory without drag," *Astronomical Journal*, Vol. 64, No. 1274, 1959, pp. 378–397.

[26] R. A. Broucke, "Long-Term Third-Body Effects via Double Averaging," *Journal of Guidance, Control, and Dynamics*, Vol. 26, No. 1, 2003, pp. 27–32.

[27] T. Guffanti and S. D'Amico, "Linear Models for Spacecraft Relative Motion Perturbed by Solar Radiation Pressure," *Journal of Guidance, Control, and Dynamics*, 2019, pp. 1–20.

[28] M. Willis and S. D'Amico, "Fast Angles-Only Relative Navigation Using Polynomial Dynamics," *11th International Workshop on Satellite Constellations and Formation Flying*, Milano, Italy, 2022.

[29] T. Delabie, J. De Schutter, and B. Vandenbussche, "An Accurate and Efficient Gaussian Fit Centroiding Algorithm for Star Trackers," *The Journal of the Astronautical Sciences*, Vol. 61, 2014, pp. 60–84.

[30] D. Mortari, M. A. Samaan, C. Bruccoleri, and J. L. Junkins, "The Pyramid Star Identification Technique," *Navigation*, Vol. 51, No. 3, 2004, pp. 171–183.

[31] J. R. Wertz, *Spacecraft Attitude Determination and Control*. Springer Science & Business Media, 2012.

[32] D. Reid, "An Algorithm for Tracking Multiple Targets," *IEEE Transactions on Automatic Control*, Vol. 24, No. 6, 1979, pp. 843–854.

[33] M. Chernick and S. D'Amico, "New Closed-Form Solutions for Optimal Impulsive Control of Spacecraft Relative Motion," *Journal of Guidance, Control, and Dynamics*, Vol. 41, No. 2, 2018, pp. 301–319.

[34] J. Sullivan and S. D'Amico, "Adaptive Filtering for Maneuver-Free Angles-Only Navigation in Eccentric Orbits," *27th AAS/AIAA Space Flight Mechanics Conference*, San Antonio, TX, 2017.

[35] N. Stacey and S. D'Amico, "Autonomous Swarming for Simultaneous Navigation and Asteroid Characterization," *AAS/AIAA Astrodynamics Specialist Conference*, Snowbird, UT, 2018.

[36] Y. Hu, I. Sharf, and L. Chen, "Distributed orbit determination and observability analysis for satellite constellations with angles-only measurements," *Automatica*, Vol. 129, 2021.

[37] R. L. Cognion, "Large phase angle observations of GEO satellites," *Sensors and Systems for Space Applications VI* (K. D. Pham, J. L. Cox, R. T. Howard, and G. Chen, eds.), Vol. 8739, International Society for Optics and Photonics, SPIE, 2013, pp. 194–205.

[38] C. Beierle and S. D'Amico, "Variable Magnification Optical Stimulator for Training and Validation of Spaceborne Vision-Based Navigation," *Journal of Spacecraft and Rockets*, Vol. 56, No. 4, 2019, pp. 1060–1072.